Soft Matter

PAPER

View Article Online
View Journal

Cite this: DOI: 10.1039/d6sm00020g

Multiscale structural–rheological mapping of cancer spheroids during maturation

Kajangi Gnanachandran, †*[ab] Massimiliano Berardi, †[cd] Grażyna Pyka-Fościak, [e] Joanna Pabijan,[b] B. Imran Akca‡[d] and Małgorzata Lekka ‡[b]

Received 8th January 2026,
Accepted 2nd June 2026

DOI: 10.1039/d6sm00020g

rsc.li/soft-matter-journal

Recent studies highlight the central role of mechanical properties in understanding solid tumor biology, progression and therapeutic response. However, the mechanical characterization of 3D *in vitro* tumor models such as cancer spheroids remains incomplete. Current experimental and modeling frameworks often overlook their spatially varying and multiscale features, limiting a unified understanding of how spheroid structure governs mechanical response. Here, we combine atomic force microscopy and hydraulic force spectroscopy to perform multiscale microrheology of cancer spheroids, probing their mechanical evolution at both single-cell and multicellular levels over time. We identify a characteristic power-law behavior whose parameters capture contributions from intra- and inter-cellular mechanics, and we relate these parameters to structural organization and its temporal progression. This structure–rheology framework provides a mechanistic view of spheroid maturation and establishes a platform for future studies on tumor mechanobiology, therapy response, and engineered microenvironments.

1 Introduction

The field of mechanobiology has garnered increasing attention in recent years, as quantification of the viscoelastic properties of cells and tissues has helped to understand cellular fate,[1] tissue formation,[2] and provided ways to distinguish between healthy and diseased cells.[3] Mechanomarkers have also shown promise in studying tissue-level pathologies.[4,5] For example, nanoindentation devices used for breast tumor screening have reached the stage of clinical trials.[6] Among the various techniques employed, atomic force microscopy (AFM) has emerged as a key surface-based method for cellular mechanics at the nanoscale. This approach has proven particularly valuable in bladder cancer, with AFM measurements consistently demonstrating that non-malignant cells are stiffer than their malignant counterparts.[7–9] Building on this foundation, we recently demonstrated that rheological mechanomarkers can discriminate more effectively between cells at various stages of bladder cancer progression, with similar, but not fully overlapping, mechanical trends observed in single cells and multicellular spheroids.[10]

Although the use of spheroids has increased considerably in recent years to study cell–cell and cell–extracellular matrix (ECM) interactions in 3D, as well as the interplay between cellular mechanics, ECM mechanics and drug diffusion,[11–14] their full potential remains underexplored in the context of mechanobiology. In particular, the relationship between the mechanical properties of individual cells, the dynamic behavior of cancer cells within a 3D cluster, and the mechanics of cell–ECM interfaces is sparsely documented.

Recent studies show that relying on easily accessible metrics, such as spheroid size, poorly predicts internal features, including necrotic zones. In contrast, internal structural[15–17] and mechanical[18] analysis provide more meaningful insights. Spheroid mechanics cannot be inferred from size or structure alone. Internal structural variations such as necrosis, ECM deposition, and cell-density gradients create mechanical heterogeneity that nano scale and bulk measurements miss. Since key biological processes in 3D cultures – metabolism, gene and protein expression, drug response – depend heavily on these mechanical microenvironments, there is a pressing need for methods that can simultaneously measure mechanical properties across the scales where these processes operate.

Currently, the field still lacks methods that can capture the multi-scale mechanical complexity of 3D cancer models. As highlighted by two recent reviews,[19,20] existing mechanical

[a] *Vascular Biology Research Group, Department of Medical Biology, UiT – The Arctic University of Norway, Tromsø, Norway. E-mail: g.kajangi@gmail.com*
[b] *Institute of Nuclear Physics, Polish Academy of Sciences, Kraków, PL-31342, Poland*
[c] *Optics11 life B.V., Hogehilweg 1, Amsterdam 1101CA, The Netherlands*
[d] *LaserLab, Department of Physics and Astronomy, Vrije Universiteit Amsterdam, De Boelelaan 1081, Amsterdam 1081HV, The Netherlands*
[e] *Department of Histology, Jagiellonian University Medical College, Kopernika 7, Kraków 31-034, Poland*
† These authors contributed equally to this work.
‡ These authors jointly supervised this work.

testing techniques are divided into surface methods, such as AFM,[10] and bulk methods, such as parallel plate compression.[21] Each provides useful isolated measurements but neglects the stratified, multi-scale nature of the 3D samples.

To address this, we present a multiscale microrheology approach that enables mechanical profiling of cancer spheroids at both single-cell and local multicellular cluster scales, paired with quantitative histological analysis and confocal imaging. Using AFM for nanoscale mechanics and hydraulic force spectroscopy (HFS)[22] for cluster-level measurements, we study spheroids representing different stages of bladder cancer progression. These rheological measurements, conducted *via* dynamic mechanical analysis (DMA) and creep, are paired with detailed histological and confocal analyzes of the inner structures of the spheroid. Our findings reveal a distinct mechanical behavior for each type of spheroid under investigation and demonstrate strong correlations between mechanical heterogeneity, the presence of ECM and cellular organization, highlighting that treating spheroids as homogeneous entities leads to an incomplete understanding of their biomechanical behavior. We show that spheroids exhibit power-law rheology across multiple scales and how such models depend on the scale of interaction. Given its label-free nature and rapid execution, our combined approach holds promise for broader application in fundamental mechanobiology and drug screening platforms.

2 Materials and methods

2.1 Spheroid culture

We cultured spheroids from three cell lines: HCV29 – non-malignant transitional cell carcinoma of the ureter (established at the Institute of Experimental Therapy, PAN, Wroclaw, Poland),[23] T24 – transitional cell carcinoma from ATCC (LGC Standards, Poland)[24] and HT1376 – grade III urinary bladder cell carcinoma from ATCC (LGC Standards, Poland).[25] Among the malignant cell lines, T24 is considered more aggressive than HT1376, reflecting its higher invasive potential.[26] HCV29 and T24 were cultured in Roswell Park Memorial Institute Medium (RPMI) 1640 medium (Sigma-Aldrich, Poznań, Poland) supplemented with 10% of fetal bovine serum (FBS, Sigma-Aldrich, Poznań, Poland). HT1376 were grown in Eagle's minimum essential medium (EMEM, LGC Standards, Poland) with 10% FBS. All cell lines were grown in culture flasks (Sarstedt, Germany) in an incubator (Nuaire, USA) at 37 °C in a 95% air and 5% CO_2 atmosphere. We kept the relative humidity above 98% and performed cell passaging at 80–90% of the confluency level. For HCV29 and T24 cells, 0.05% and for HT1376 cells, 0.25% trypsin-EDTA solution (Sigma-Aldrich, Poznań, Poland) was applied. After a few passages (<10), the cells were ready to seed in 96-well U-bottom 3D cell culture plates (Thermofisher). Depending on the cell line, the number of cells per well was adjusted to obtain spheroids of 350–400 μm diameter (for HCV29 spheroids: 7000 cells per well, for T24 spheroids – 10 000 cells per well and for HT1376 spheroids – 1500 cells per well were used). To ensure comparable spheroid size across cell lines, all subsequent measurements, including fusion assays and HFS, were normalized to spheroid diameter to account for any residual size differences.

2.2 AFM microrheology

To immobilize the spheroids prior to indentation, we coated Petri dishes with 0.01% poly-L-lysine (Sigma-Aldrich, Poznań, Poland) and 5% glutaraldehyde (Sigma-Aldrich, Poznań, Poland). Briefly, we cleaned the Petri dish using ethanol and deionized water and dried it, incubated it with diluted glutaraldehyde for 20 minutes, followed by a wash with water. Afterward, we placed the diluted poly-L-lysine for 30 minutes, removed the solution, and let the dish dry. At this point, it was ready for use. We collected the spheroids from the culture plates and placed them on the coated dishes. Before starting a measurement, we waited 15–30 minutes to ensure that spheroids adhered to the poly-L-lysine-coated surface. We conducted the microrheological measurements using a NanoWizard IV (Bruker, JPK Instruments) in PBS and at room temperature. We used an NSC36 cantilever (0.6 N m^{-1}, tip height 12–18 μm and half-open angle of 20 degrees). We set the approach velocity at 3 μm s^{-1} and the force set point at 30 nN. A high force set point enables to probe deeper regions of the spheroids, up to ≈3 μm. Since such a threshold may lead to membrane ruptures, we inspected every curve and analyzed only those that complied with the Hertzian response. An example of the recorded force curve is shown in the Fig. S2-a. The dynamic response was set between 1 and 250 Hz in 9 logarithmically evenly spaced frequencies. The following parameters were set: a constant oscillation amplitude of 50 nm for 10 oscillations, sampling 600 points per period, and waiting 0.5 seconds between test frequencies. We collected the measurements in a series of matrices (9 μm^2, 2 maps/spheroid), on 12–15 spheroids per type and time point. We did not apply any hydrodynamic drag correction. We qualitatively inspected the need for it by observing the separation between approach and retract curves in a quasi-static indentation at comparable velocities, and we found the baselines to be essentially overlapping. This may be due to the relatively high tip length, spheroid curvature, and soft substrate. Moreover, using the cantilever parameters (k = 0.6 N m^{-1}, f_0 = 27.5 kHz, Q = 3), the estimated hydrodynamic damping coefficient was on the order of 10^{-6} kg s^{-1}, indicating a small contribution to the measured dissipative response under the experimental conditions used here. Since AFM is used here primarily for relative comparisons between the three spheroid lines, the lack of hydrodynamic correction does not affect the interpretation of differences between cell lines.

We analyzed the raw data in JPK Data Processing using the Hertzian contact model for a pyramidal indenter with blunted end assuming a conical shape (for details, see the supplementary methods – AFM modeling). We assumed spheroids to be incompressible.

2.3 HFS microrheology

Because HFS measurements work on suspended bodies, we simply transferred the spheroids from their culture well plates to Petri dishes. We used the HFS device in a configuration described previously,[22,27] using nozzles with 52–60 μm diameter.

We performed the measurements in PBS (Phosphate-Buffered Saline, Sigma-Aldrich, Poznań, Poland), at room temperature. To avoid effects arising from cell death, we performed the experiments in small sets of 4–5 spheroids, which would typically take 30–40 minutes to complete. Between each set of measurements, we washed the tip with a 10% solution of helyzime (Braun, Germany), isopropanol (Sigma-Aldrich, Poznań, Poland) and deionized water. Whenever we observed cell debris within the nozzle that could not be removed by washing, we sonicated the tip for about 20 seconds, in isopropyl alcohol followed by deionized water. We ran all the experiments in pressure control, with an aspiration pressure set point of 300 Pa and a suction rate of 50 Pa s^{-1}, held for 20 s prior to the oscillation phase. We measured the dynamic response between 0.05 and 20 Hz, in 9 log-evenly spaced frequencies. We set a constant pressure oscillation amplitude of 50 Pa, waiting 2 seconds in between oscillations. We collected data for each spheroid in 4 well-separated locations, releasing and recapturing them with the help of the pressure controller and a micromanipulator to reposition the suction tip. Test parameters were chosen as a compromise between a good SNR for interferometric detection, and the goal of performing a minimally invasive mechanical test with strain $\varepsilon < 10\%$. We calculated the complex modulus E^* as we detailed in a previous work,[27] using the equation:

$$E^* = \frac{3R_p}{\beta_1\left[1-\left(R_p/R_c\right)_3^{\beta}\right]} \cdot \frac{P_0}{L_0} \cdot e^{i(\delta_P-\delta_L)} \quad (1)$$

where R_p is the radius of the pipette (between 52 and 60 μm), R_c is the radius of the sample, $\beta_1 = 2.0142$, $\beta_3 = 2.1187$, P_0 and L_0 are the pressure amplitude and aspirated length, respectively, and δ_P and δ_L their respective phase changes at a given frequency. We corrected for hydrodynamic drag and analyzed the data as described in our previous work,[22] ensuring that dissipative interactions are properly captured across the full frequency range. This allows reliable quantification of both storage and loss moduli at the cluster scale. An example of the raw data is shown in the Fig. S2-b. We assumed spheroids to be incompressible.

2.4 Dynamic mechanical analysis (DMA) modeling

We imported the results (storage, loss, and corresponding frequency values) of both AFM and HFS in Python to fit the full set of measurements per line/day to two lumped parameter models. For AFM, we used two springpots in parallel,[28] which describe the complex modulus dependence on frequency as:

$$E^*_{AFM}(\omega) = c_\alpha(i\omega)^\alpha + c_\beta(i\omega)^\beta \quad (2)$$

where α and β are the indices of the derivation of the two springpots (between 0 and 1), c_α and c_β their associated parameters and ω the applied frequency.[28]

For HFS, we used the AFM lumped parameters at the starting point and added a dashpot in series to represent cell–cell and cell–ECM interfaces. The equation of the model takes the form:[28]

$$E^*_{HFS}(\omega) = \frac{\eta(i\omega)\cdot\left[c_\alpha(i\omega)^\alpha + c_\beta(i\omega)^\beta\right]}{\eta(i\omega) + c_\alpha(i\omega)^\alpha + c_\beta(i\omega)^\beta} \quad (3)$$

where, analogously to the AFM fit, α, β, are indices of derivation for two springpots, with c_α and c_β their associated terms, and η is the dashpot viscosity.

In both cases, we weighted the frequency terms using the inverse of standard errors. We assessed the quality of the fits with χ^2, which averaged at 2.9, indicating a good result. We computed the 95% confidence intervals using block bootstrapping, using 6000 simulations.[29] To verify the need for a fractional model, we first defined a classic Burgers model,[30] ran the optimization procedure, and visually compared the result to the output of the fractional model. The Lumped parameter models composed of only springs and dashpots systematically failed to capture the storage and loss moduli (data available in the SI, Fig. S3. Average χ^2 of 18.7).

2.5 Cytochalasin-D treatment and time-domain viscoelastic modeling

At day 3 of spheroid culture, we placed the spheroids in PBS containing 5 μM cytochalasin D (Cyto D, Sigma-Aldrich, Poznań, Polska) for 30 min at 37 °C. We then carefully washed the spheroids and added fresh culture medium before proceeding with the experiments.

We conducted time-domain viscoelasticity experiments with HFS alone, using a ramp-and-hold profile identical to the DMA one. We collected between 24 and 40 creep curves (well separated on the spheroid surface, as described above) on at least 10 spheroids per condition. We modeled the data *via* numerical integration using RHEOS,[31] with the same lumped parameter model found after DMA measurements. As RHEOS requires stress–strain relationships to fit the models in its library, we used the suction pressure as applied stress (expressed in Pa) and approximated the radial strain as $\delta R/R_c$, with δR representing the aspirated length of the spheroid in the micropipette.

2.6 Spheroid fusion

For the spheroid fusion experiments, we prepared spheroids from the three types of bladder cell lines as described above. After 3 days of culture, we placed the spheroid pair in a new well, with the corresponding fresh culture medium for each cell line. We determined the degree of fusion of homotypical spheroids after 24 hours from their first contact. To obtain the degree of spheroid fusion, we fit a circle to each spheroid and calculated the angle θ between the line connecting the centers of the circles and the line passing through one of the circles and one of their intersection points (*i.e.*, the fusion neck). We calculated the degree of fusion as $\sin^2\theta$.

2.7 Histology

We collected spheroids that were cultured for 3 and 14 days in 1.5 ml Eppendorf tubes. We fixed the samples with 10% neutral buffered formalin (Sigma-Aldrich, Poznań, Polska) for 15 minutes. We dehydrated the samples in a series of diluted alcohol solutions: 50%, 80%, 96% and 100%. Each dehydration step lasted 15 minutes. We then treated the samples with xylene (Sigma-Aldrich, St. Louis, MO. USA), removed it, and embedded the spheroids in paraffin blocks. We cut 6 μm thick slices using a

microtome (Biocut 2035, Leica Instruments GmbH) and mounted them on poly-L-lysine-coated slides (Menzel-Glaser, Thermo Scientific).

The deparaffinized sections were stained with hematoxylin and eosin, as well as using histochemical methods: Masson's trichrome to distinguish cells from the surrounding connective tissue and Sirius Red stain to qualitatively assess the spatial distribution of collagen-rich ECM across superficial and deeper spheroid regions, to check their possible correlations with nanomechanical and rheological changes in bladder spheroids.

Example of the full slices are shown in Fig. S7–S9.

2.8 Quantitative histology

We performed a quantitative analysis of the H&E staining using a pre-trained convolutional neural network (Stardist 2D, Versatile H&E model[32]), accessed through ImageJ. An example of the segmentation result is available in the Fig. S10. We extracted the coordinate list, area, perimeter, aspect ratio, and circularity for each of the nuclei. We imported the results into MATLAB R2022b for further processing. We iteratively selected the outermost set of nuclei and recorded their average feature, as well as the distance from the initial set boundary. We then grouped the nuclei in three sets, under the assumption that the first 25 μm contain mainly proliferating cells, and that beyond 100 μm nutrients have a lower concentration. In practice, as expected, both the aspect ratio and the area vary continuously, both in the radial and tangential directions (see Fig. S11). However, the dependence of AR as a function of the radial position is apparent in all lines. We repeated the procedure on two slides for each condition and found the results to be very consistent. We calculated the 3 to 14 day compaction as:

$$\frac{N_{14}}{N_3} \tag{4}$$

where N is the density of nuclei per μm^2 at 14 and 3 days, as denoted by the subscripts. We estimated the area of each region using the boundary definition described above. We compared the aspect ratio of the nuclei in between regions for each spheroid as a proxy of cell shape, using a Mann–Whitney U test.

2.9 Confocal imaging

We used the following protocol to stain spheroids at 3 and 14 days: we collected the samples in 1.5 ml Eppendorf tubes and fixed them in 3.7% PFA for an hour. The samples were then treated with 1% cold Triton X-100 overnight at 4 °C, washed three times in PBS for two minutes each and then washed once more in PBS. Then we added 1% cold BSA solution, for 3 hours at 4 °C. Once again, we washed the samples in PBS. Next, we incubated the spheroids overnight at 4 °C with phalloidin conjugated with Alexa Fluor 488 (1 : 20, in PBS). The following day, we substituted the dye with Hoechst 33342, diluted 1 : 5 in PBS, and incubated in the same way. The following day, we washed the samples in PBS, moved them to an 18 well glass bottom slide (Ibidi), with the addition of an anti-shading solution (Thermo Fisher) with the same refractive index as the oil used for the immersion objective (1.52). We recorded the images using a Leica TCS SP8 WLL confocal microscope, using a 63× objective lens (HC PL APO CS2, NA 1.40).

3 Results and discussion

In this study, we prepared multicellular spheroids using three bladder cancer cell lines representing different tumor stages: non-malignant HCV29 cells (from the non-cancerous part of bladder carcinoma that features the morphology and properties of the normal epithelium), HT1376 cells (grade III bladder carcinoma), and T24 cells (grade III transitional cell carcinoma). We performed a dynamic mechanical analysis (DMA) using both AFM and HFS, to characterize their rheological responses at the cellular and cluster levels. Measurements were conducted after 3 days and 14 days of culture to evaluate changes in their biophysical properties during maturation over time, with the two time points chosen to represent two distinct stages of growth.[17] The HCV29 and T24 spheroids gradually shrank from day 3 and reached a plateau over the course of about a week, whilst HT1376 continued to grow at a steady pace. All three types of spheroids exhibited a high level of circularity, with a median value of ≈ 0.9, and minor variations between 3 and 14 days (see supplementary methods – Brightfield image analysis and Fig. S1-a and b).

3.1 Rheology of spheroids follows time and scale dependent power laws

To determine whether spheroid mechanics depends on both spatial scale and maturation stage, we first compared AFM and HFS frequency responses across the three cell lines. The experimental workflow for AFM and HFS is represented in Fig. 1-a, while Fig. 1-b illustrates the indentation scales through finite element modeling (obtained *via*[22]), supported by and example of histological labeling of an indented spheroid fragment. As the finite elements colour maps show, the two methods are averaging the response of drastically different volumes: in AFM-based nanoindentation, mechanics is predominantly dependent on the cytoskeleton of cells at the surface of the spheroid, and the volume average is dependent on the applied load. Conversely, in HFS the averaged volume can be approximated to a cylinder of radius R_p equal to that of the pipette, and height $\approx 1.5R_p$, in line with previous reports.[33] As the aspirated area is constant, the affected volume is independent of the suction pressure. Given our R_p of 25 μm, HFS averages the response of about 100 cells (under the simplifying assumption they are spherical and 10 μm in radius). This multiscale framework enables comparison of mechanical responses at different structural levels and their evolution over time. Beyond the fitted parameters, the experimental rheological spectra (Fig. 1-d) show that maturation alters the balance between storage and loss responses differently across scales. AFM measurements reveal stronger high-frequency solid-like behaviour at the spheroid surface, whereas HFS captures broader low-frequency dissipation associated with collective rearrangements and multicellular stress relaxation.

The viscoelastic response of spheroids under AFM indentation was described using a model composed of two springpots

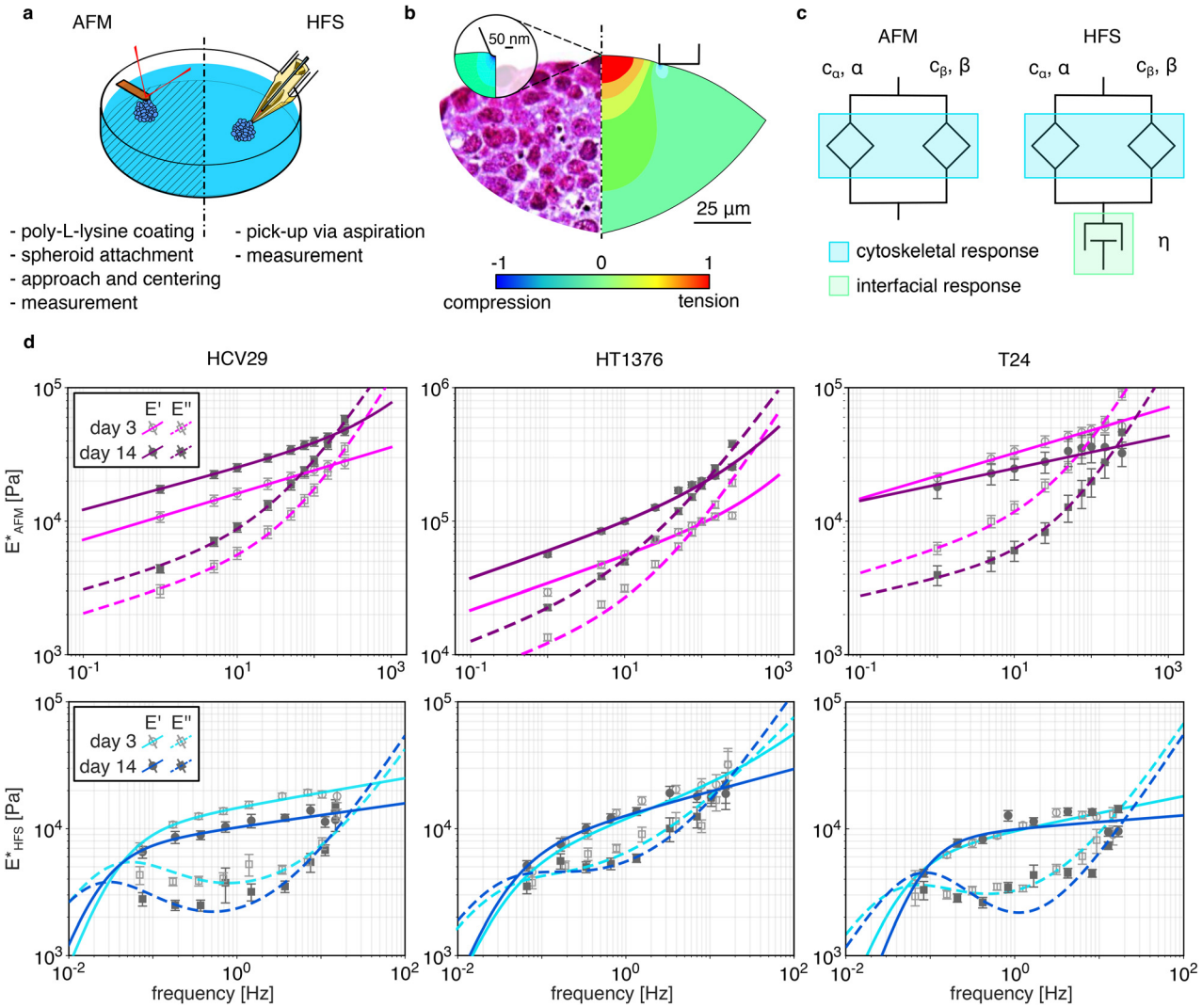

Fig. 1 Spheroid microrheology at the cell (AFM) and cluster (HFS) scales and their evolution in time. (a) Schematic of the workflow for the AFM and HFS approaches. (b) Normalized displacement vector sum from FE models, showing the scale of indentation in spheroids (left – a histologically labeled fragment of the indented spheroid (HT1376 day 3); right – finite element simulation). (c) Schematic representation of the lumped parameter models used. On the left, the equivalent of a double power law used to fit AFM data, and on the right the same model with the addition of a dashpot in series used to fit HFS data. (d) Microrheology results at both cell (AFM) and cluster (HFS) scales. Data points, expressed as mean ± SEM are shown as circles (storage modulus) and squares (loss modulus). Solid and dashed lines indicate the best fit for storage and loss moduli, respectively. In all cases, a light tint (fuchsia, turquoise) indicates day 3, and a dark tint (purple, blue) day 14. For each spheroid type, we performed n_{HFS} = 39–46 measurements on N = 10–12 different spheroids, and n_{AFM} = 280–350 measurements on N = 10–13 spheroids.

arranged in parallel[28] (Fig. 1-c), designed to capture both short- and long-timescale relaxation dynamics. The data was well described by this approach (Fig. 1-d), consistently reflecting the characteristic dual power-law behaviour of cytoskeletal mechanics reported in several other studies.[10,34,35] To evaluate the transition from solid-like to liquid-like regimes, we computed the transition frequency, defined as the frequency at which the storage modulus (E') equals the loss modulus (E''), marking a shift in dominance from elastic to viscous response. A similar metric has been reported in previous AFM studies on T24 spheroids,[36] where transition frequencies were associated with collagen-dependent mechanical changes. While a direct quantitative comparison is not straightforward due to differences in modelling approaches, tip shape and experimental focus, the comparable range of transition frequencies supports the consistency of the observed viscoelastic behaviour across independent studies (between 170 and 197 Hz in ref. 36 *vs.* 128 Hz in the present study).

Over time, the mechanical response of the HCV29 and HT1376 spheroids shifted towards increased stiffness, with E' and E'' increasing by approximately 1.5-fold and 2-fold, respectively, while the viscous losses (expressed as phase lag; see Fig. S4) remained largely unchanged. As a result of this, their transition frequencies showed only minimal shifts over time: from 178 Hz to 187 Hz for HCV29 spheroids and from 94 to 110 Hz for HT1376 spheroids. In contrast, T24 spheroids exhibited a markedly different evolution. Their mechanical response became less dependent on the frequency, with apparent softening at higher frequencies.

Simultaneously, the viscous losses decreased significantly, leading to a more solid-like behavior. This shift was reflected in a pronounced increase in the transition frequency, from 128 Hz on day 3 to 210 Hz on day 14.

The results at the cluster level obtained through HFS (Fig. 1-d, bottom row) differed substantially from those observed on the cellular scale. Across all three spheroid lines, the storage-to-loss modulus ratio evolved in a non-monotonic fashion, indicative of viscoelastic liquid-like behaviour. Initial attempts to fit the DMA data using the traditional lumped-parameter models typically used to characterize spheroid rheology[21,30,37–39] were unsuccessful (see Fig. S3), and in line with recent observation from Pandey *et al.*[40] As models featuring discrete relaxation times cannot reproduce the continuous power-law scaling observed in the experimental trends, we adopted a fractional viscoelastic model composed of two parallel springpots, representing the cellular components as in the AFM analysis, connected in series with a dashpot to describe the dissipative interactions at the cell–cell and cell–ECM interfaces (Fig. 1-c). This addition is necessary compared to the AFM tests, as during aspiration the spheroid is under tension, and the interfaces play a key role in load transfer. This model was able to accurately reproduce the observed behaviour and revealed two characteristic crossover frequencies between solid-like and fluid-like behaviour: one at very low frequencies (0.02–0.08 Hz) and one at high frequencies (10–30 Hz).

HCV29 spheroids progressively softened over time, with viscous losses decreasing disproportionately at low frequencies and increasing at high frequencies. This resulted in a shift of both transition frequencies, from 0.043 Hz to 0.026 Hz and from 50 to 23 Hz, respectively. HT1376 spheroids showed the most liquid-like behavior, as evidenced by the small separation between storage and loss moduli between the low (0.056 Hz) and high (28 Hz) transition frequencies. Temporal changes were mainly confined to higher frequencies (>3 Hz), where the reduced frequency dependence of E' led to a lower high-frequency transition (13 Hz), while the low-frequency transition remained nearly unchanged (0.053 Hz). Lastly, T24 spheroids showed limited mechanical changes over time, with viscous losses decreasing by $\approx 25\%$ at their lowest point, which is more evident in phase lag (see the Fig. S4, bottom right panel). They were also characterized by the smallest shifts in transition frequencies, from 0.059 Hz and 18 Hz at day 3 to 0.083 Hz and 20 Hz at day 14. Interestingly, among the three spheroid lines, the dashpot viscosity ranked HCV29 $>$ HT1376 $>$ T24 (see the η parameter in Table 1), reflecting an inverse correlation between viscosity and tumor aggressiveness. This ranking was consistent at both time points, with an increased separation between the values (from a 2-fold to 3-fold change between the dashpot viscosities of HCV29 and T24 at the two time points).

When comparing the two different scales, AFM and HFS, the mechanical responses appear markedly different across all spheroid lines and time points, both visually and in terms of lumped parameter model fit values. In our previous work[22] we showed how the two approaches, when applied to homogeneous materials whose mechanical response is not scale-dependent, yield equivalent results. This implies that here the discrepancies relate to different mechanical responses, which is consistent with previous work.[41] Considering the inherent differences in the spheroid architecture and spatial scale, the direction of testing, and control modalities between the two measurement techniques, this is hardly surprising.

However, some common traits emerge. In particular, the frequency-dependent stiffening classification is preserved: the T24 spheroids show the mildest change of $E'(\omega)$, followed by HCV29 and HT1376. The power law dependency in α, whilst differing in magnitude, ranked the lines in the same way across the scales. On day 3, both AFM and HFS showed similar values for the HCV29 and T24 spheroids, with the HT1376 spheroids retaining the higher value. On day 14, both methods reported $\alpha_{HT1376} > \alpha_{HCV29} > \alpha_{T24}$. The marginal inconsistency at an early time may be due to a not-yet settled spheroid structure, with differences stemming from interfacial contributions. Viscous losses around 1 Hz were also remarkably consistent between the two scales, across all lines, and over time. Moreover, both methods found the optimal fits for fractional exponents in the

Table 1 Results of the DMA fit for AFM (parallel springpots), and HFS (parallel springpots plus dashpot in series), and associated solid–liquid transition frequencies for both measurement days. Results are shown as best fit ± 95% confidence interval, obtained *via* block bootstrapping (6000 resamples)

Condition	c_α [Pa s$^\alpha$]	α [—]	c_β [Pa s$^\beta$]	β [—]	η [Pa s]	$\omega_{t,1}$ [Hz]	$\omega_{t,2}$ [Hz]
HCV29 spheroids							
AFM/3	8158^{+956}_{-1112}	$0.174^{+0.006}_{-0.007}$	17^{+2}_{-3}	$1.00^{+0.00}_{-0.01}$	—	—	178
HFS/3	$12\,361^{+1244}_{-850}$	$0.11^{+0.02}_{-0.03}$	61^{+23}_{-17}	$1.00^{+0.00}_{-0.00}$	$48\,743^{+14\,865}_{-11\,360}$	0.043	50
AFM/14	$13\,489^{+1621}_{-1539}$	$0.155^{+0.003}_{-0.003}$	64^{+19}_{-17}	$0.89^{+0.03}_{-0.02}$	—	—	187
HFS/14	8819^{+1257}_{-980}	$0.09^{+0.03}_{-0.02}$	83^{+21}_{-19}	$1.00^{+0.00}_{-0.00}$	$54\,484^{+22\,280}_{-14\,523}$	0.026	23
HT1376 spheroids							
AFM/3	$20\,787^{+2607}_{-2727}$	$0.254^{+0.008}_{-0.007}$	94^{+11}_{-11}	$1.00^{+0.00}_{-0.00}$	—	—	94
HFS/3	8843^{+1210}_{-3073}	$0.23^{+0.10}_{-0.16}$	308^{+2743}_{-255}	$0.76^{+0.16}_{-0.34}$	$32\,198^{+85\,817}_{-10\,982}$	0.056	28
AFM/14	$41\,150^{+2795}_{-2909}$	$0.220^{+0.004}_{-0.005}$	546^{+89}_{-81}	$0.85^{+0.01}_{-0.01}$	—	—	110
HFS/14	9935^{+1039}_{-904}	$0.18^{+0.03}_{-0.02}$	177^{+42}_{-44}	$1.00^{+0.00}_{-0.00}$	$44\,070^{+13\,375}_{-6548}$	0.053	13
T24 spheroids							
AFM/3	$16\,577^{+3146}_{-3178}$	$0.171^{+0.007}_{-0.006}$	45^{+9}_{-9}	$1.00^{+0.00}_{-0.00}$	—	—	128
HFS/3	7937^{+752}_{-660}	$0.13^{+0.02}_{-0.02}$	102^{+24}_{-20}	$1.00^{+0.00}_{-0.00}$	$26\,722^{+3724}_{-5682}$	0.059	18
AFM/14	$15\,336^{+3326}_{-4052}$	$0.122^{+0.005}_{-0.007}$	22^{+6}_{-7}	$1.00^{+0.00}_{-0.00}$	—	—	211
HFS/14	9269^{+500}_{-838}	$0.05^{+0.02}_{-0.02}$	87^{+9}_{-9}	$1.00^{+0.00}_{-0.00}$	$19\,078^{+1208}_{-2234}$	0.083	20

range $\alpha < 0.25$ and $\beta \approx 1$. The former is aligned with previous measurements in other epithelial lines.[42,43] The β exponent was mostly equal to 1, indicating purely dissipative behavior at high frequency, with the only exception being the HT1376 spheroids.

In practical terms, AFM primarily reports how individual surface cells resist deformation through cytoskeletal relaxation, whereas HFS captures how groups of cells collectively dissipate stress through intercellular rearrangements and interface-mediated flow. The preservation of fractional power-law behaviour across both scales suggests that the same broad viscoelastic principles govern the system, while the different transition frequencies reveal how these mechanisms manifest differently at the single-cell and multicellular levels.

3.2 Dynamic aspiration captures rheological traits of both cytoskeleton and cellular interfaces

As the microscale rheology of spheroids remains less explored, we focused on this regime to better understand which mechanical features are captured across different frequency bands. Fig. 2 shows the viscous losses, both measured and modeled on the two scales, expressed as the phase angle for the T24 spheroids on day 3. Although the figure highlights only a single spheroid line and a time point, the observed trends were consistent across all types and time points of spheroids (see Fig. S4).

From this plot, the increase in viscous losses at low frequency under HFS becomes particularly evident. The solid-to-liquid transition observed in HFS at higher frequencies shows a slope similar to that of AFM, which is expected given the similarity in power-law behaviour. However, the transition occurs at considerably lower frequencies in HFS. A recent study[44] reported that multicellular tissues, such as a spheroids, can exhibit poroelastic behaviour. Because poroelastic effects depend on fluid redistribution over characteristic length scales, they could in principle contribute differently to AFM and HFS measurements due to the substantially larger probed volume in HFS. However, in our case, we excluded it as the primary source of the discrepancy based on two observations. First, analyzing the phase angle as a function of the area-corrected characteristic frequency,[45] one can see no meaningful collapse on a master curve (see Fig. S5). Second, in our previous work on the sensitivity of HFS to poroelastic relaxation,[22] conducted with an equivalent AFM tip and HFS pairing as the one used here, we observed similar viscous losses in the overlapping frequency range. This asymmetric behavior is also in line with what was reported in another study.[46] We therefore attribute the observed behaviour predominantly to viscoelastic effects, with the discrepancy possibly tied to an asymmetric mechanical response.

The low-frequency transition is dominated primarily by the dashpot term, though parallel springpots also play a role. Given that the associated time scale is comparable to that of collective cell movement,[47,48] we hypothesized that this transition could reflect the unjamming transition and cell motility within the spheroid,[49] serving as a potential indicator of overall tissue fluidity. To further investigate this hypothesis, we performed a homotypic spheroid fusion experiment (Fig. 3). In such systems, the rate of neck formation follows $r \propto \gamma/\eta$, where γ is the surface tension and η the viscosity of the spheroids.[50] This ratio, commonly known as the visco-capillary velocity,[51,52] was not directly measured in our study. Since spheroid fusion dynamics are governed by this ratio, the normalized neck size measured at 24 h should be interpreted as an effective readout of the balance between tissue cohesion and viscous dissipation, rather than a direct measure of viscosity alone. Accordingly, we reasoned that both cellular and interfacial contributions to the effective rheological response are captured in the transition frequency. Consequently, we plotted the normalized neck radius (expressed as $\sin^2(\theta)$) as a function of the squared characteristic transition time $1/\omega_{t,1}$, corresponding to the inverse of the low-transition frequencies listed in Table 1. The three spheroid lines exhibited an approximately linear relationship ($R^2 = 0.87$, slope = -0.0013 with fixed intercept at [1,0], the limit of immediate fusion for

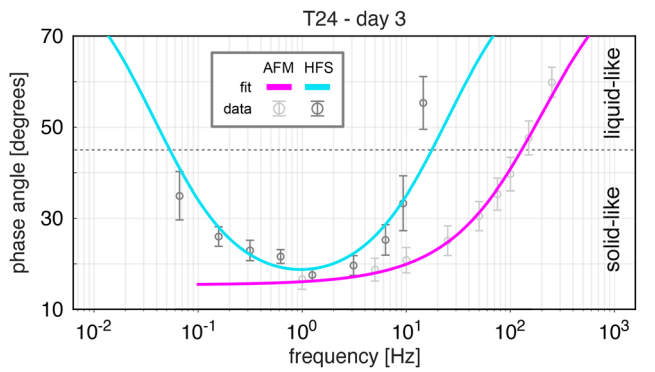

Fig. 2 Exemplary comparison of the frequency dependence of phase lag for both testing methods, expressed as mean ± SEM. At 45 degrees of phase lag, the storage and loss components equal in magnitude, representing the solid-to-liquid transition point. The modeled response (fuchsia and turquoise) using the two lumped parameter models shown in the previous figure. All three lines showed a remarkably similar look, so here we report the results for the T24 spheroids on day 3 as an example.

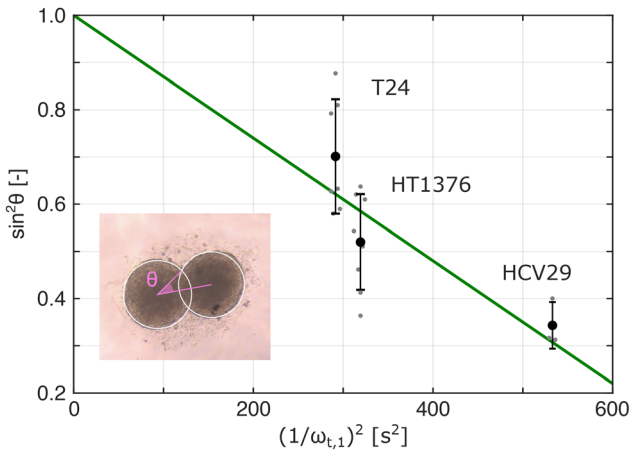

Fig. 3 Relationship between the normalized spheroid neck 24 h after fusion initiation and the lower transition frequency identified by the lumped parameter model on HFS data. Data is shown as mean ± SD, data points are horizontally shifted for visual clarity. In the inset, an exemplary image of HT1376 spheroids fusion shows how $\sin\theta$ is calculated.

spheroids with negligible viscosity) between the transition time and the degree of fusion at 24 h. This ranking remained consistent also after two weeks ($\omega_{T24} > \omega_{HT1376} > \omega_{HCV29}$, where the values are $0.088 > 0.052 > 0.026$), with an even clearer separation between the HT1376 and T24 spheroids (see Table 1, column $\omega_{t,1}$). This result, albeit limited, corroborates the idea that the dashpot term and low frequency phase transition are correlated with cellular motility. As the relation between time and fusion neck also includes γ, we estimated this value from flow asymmetry in aspiration and release, as documented in ref. 53 (see supplementary methods and Table S2). We found the surface tension values, around 2 mN m^{-1}, consistent with those of tissues, and comparable between cell lines. This suggests $\omega_{t,1}$ should be interpreted as an emergent collective property of the spheroid, reflecting the timescale of cell rearrangements and interface-mediated stress relaxation. A recent work by Boot *et al.*[53] showed how viscosity is pressure dependent, with a positive relationship. As higher viscosity would lead to longer characteristic times, it is possible that load transfer and cellular motion are load dependent.

To further clarify this connection, further tests on the individual lines following cytoskeletal contractility (for example the work done by Ongenae *et al.*[54]) would be required.

To check whether the high-frequency transition was sensitive to cytoskeletal alterations, we treated the spheroids with cytochalasin D (CytoD), performed a creep test, and modeled the results using the lumped-parameter framework previously identified during the DMA analysis. During the pressure ramping phase, the aspirated length showed a concave shape (exemplified by the T24 spheroid response shown in Fig. 4-a), which is well described by power-law behavior.[55] In the case of T24 spheroids, CytoD severely disrupted the cytoskeletal integrity by inhibiting F-actin polymerization,[10] resulting in a marked softening and a significant reduction in the high-frequency transition (Fig. 4-b). This result aligns with our previous AFM-based findings.[10] Interestingly, F-actin destabilization, on top of inducing a loss of cortical tension/structure, likely affects actin-based adherens junctions, as suggested by the observed decrease in viscosity η (for numerical results of the fit see Table S1) and the marginal shift of $\omega_{t,1}$ towards higher frequencies. The same experiment repeated on HT1376 spheroids showed the opposing effect, while HCV29 spheroids exhibited the highest degree of softening. These responses were consistent with prior AFM observations on the same spheroid types,[10] further supporting the notion that cytoskeletal integrity plays a key role in modulating rheological behavior, particularly at higher frequencies. While cortical stiffness contributes to both AFM and HFS responses, the relative weight of this contribution differs substantially between techniques. AFM is dominated by the mechanics of the superficial actomyosin cortex, whereas HFS integrates additional dissipative mechanisms arising from multicellular rearrangements, interfacial sliding, and deeper structural heterogeneity. As in HFS the load is transferred through what appear to be relatively weak interfaces, we hypothesize time dependent interfacial changes mask the cortex changes, which the CytoD data at the same time point seems to support.

In particular, whilst the material behavior is well captured, the predicted viscous losses and transition frequencies differ from those estimated during DMA (see Fig. 4-b). Because the CytoD creep data were analyzed using a simplified time-domain implementation of the lumped-parameter model, whereas the main DMA analysis was performed in the frequency domain over longer acquisition times, the absolute fitted parameter values are not expected to be numerically identical or directly comparable. The biologically relevant observation is the consistent relative downward shift in the higher transition frequency after CytoD treatment. Moreover, it is worth noting that the observations relating the fit parameter, such as the ranking of η with line aggressiveness, hold true also in this experiment. Beside the modelling aspect, it is also worth considering the lumped parameters used imply that the material is fully passive, whilst there is evidence showing cellular dynamic remodelling under uniaxial cyclic stretch.[56] Both our experiments were conducted in stress control, so the differences may be linked to the dynamic nature of DMA, or the overall duration of

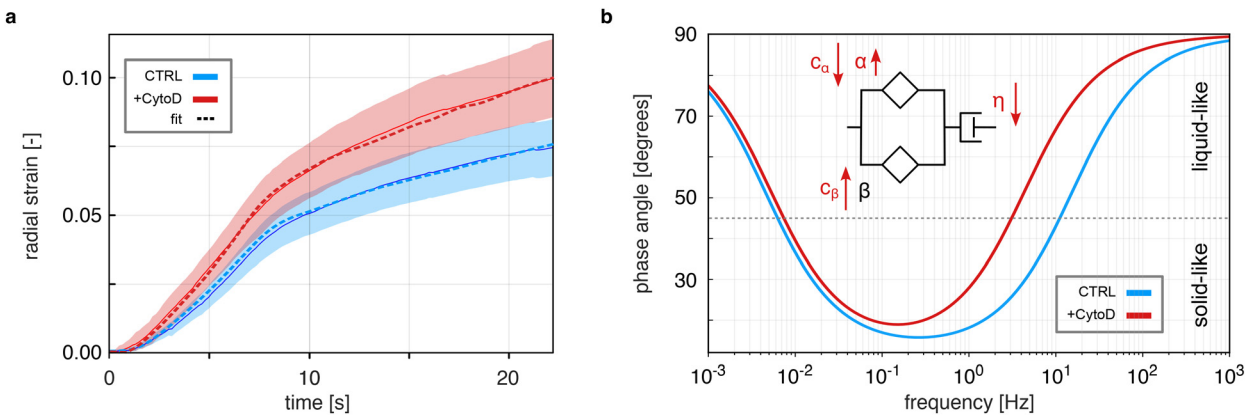

Fig. 4 Exemplary response of T24 spheroids with and without CytoD treatment. (a) Experimental result of the ramp-and-hold aspiration, expressed as radial strain in time. Data is shown as mean ± SD, and the dashed line represents the best fits from RHEOS. (b) Equivalent frequency response of the models. CytoD treatments disrupts the cytoskeleton and drastically lowers the transition frequency at which cells behave like liquids. As a secondary effect, cell–cell interfaces also appear to be affected, as the low transition frequency moves towards a shorter timescale (30% higher).

the tests (which for DMA is about 10 times longer). This discrepancy is also supported by computational approaches exploring tension-induced cytoskeletal remodeling in epithelial lines.[57,58]

Together, DMA and creep tests suggest that HFS is a suitable technique to test both cellular and interfacial rheological properties in multicellular spheroid models. Though direct numerical comparison with AFM data remains challenging due to differences in scale and loading geometry, key traits of cytoskeletal mechanics and their pharmacologically induced alterations are consistently measurable across the two methods. However, these results fail to clarify the divergent temporal trends observed in the lumped-parameter terms attributed to the cellular component. To address these discrepancies, we focused our attention on the evolving architecture of the spheroids and their influence on mechanical behavior over time.

3.3 Spheroids undergo time and layer dependent structural remodeling

To explain the divergent temporal trends observed mechanically, we finally examined how spheroid architecture remodels across depth and time. We investigated the internal structure of the spheroids by histological and confocal analyses. Histological analysis (Fig. 5-a) reveals a time-dependent reorganization in all types of spheroids. On day 3, each spheroid exhibits a proliferative outer layer and viable cells also in the inner regions. By day 14, a more defined layered structure emerges. HCV29 spheroids show moderate outer compaction and prominent collagen accumulation, mainly beneath the surface, as highlighted by Masson's trichrome and Sirius Red staining. HT1376 spheroids develop a necrotic core on day 14, likely due to sustained growth and limited access to nutrients; the vacuoles present on day 3 may be the precursor to the formation of the necrotic core. Collagen is not detected, and compaction remains minimal. The T24 spheroids display dense cell packing across the section, especially in the subsurface region. Sirius Red staining shows the early presence of collagen on day 3, which is no longer visible on day 14.

Quantitative analysis of hematoxylin & eosin (H&E) histology images (Fig. 5c–e) shows how all three types of spheroid undergo significant remodeling. An increase in nuclei density in the outer region over time and an increase in the nuclei aspect ratio (AR) were observed. Since cell–cell interactions, governed primarily by cadherins, are important for spheroid formation,[59,60] we checked the expression of N and E-cadherins using western blot (see supplementary methods – SDS-PAGE and western blot and immunodecoration and Fig. S1-c). We found that HCV29 and T24 spheroids express N-cadherin and not E-cadherin, whilst the opposite is true for HT1376 spheroids, in agreement with previous studies carried out in 2D cell cultures.[61] The distinct expression of N-cadherin in HCV29 and T24 *versus* E-cadherin in HT1376 may influence tissue mechanics by modulating the stability of intercellular junctions, affecting collective cell rearrangements and the effective low-frequency fluidity, rather than directly predicting absolute stiffness values. The time-dependent trends are particularly marked in the lines expressing N-cadherins (median AR of the proliferating layer increases $\approx$50% for both HCV29 and T24 spheroids). The only exception (lowered cell density in the inner region of HT1376 spheroids) can be related to the presence of a necrotic core. On day 14, all spheroids exhibit a statistically significant difference in the AR distribution between the inner and outer layers (Mann–Whitney *U* test), indicating the emergence of spatial heterogeneity and tissue-like organization. Confocal imaging (Fig. 5-b) reveals progressive changes in actin organization in all spheroid types. In HCV29 spheroids, actin fibers are sparsely visible on day 3, primarily localized around the cell periphery. On day 14, a stronger actin signal appears in the outer layer, with actin forming a condensed and irregular pattern. The presence of condensed nuclei suggests apoptotic activity. HT1376 spheroids exhibit well-defined cortical actin on day 3 and maintain a structured cytoskeleton on day 14. Additionally, unlike the other two cell lines, HT1376 cells are known to lack thick actin bundles,[10] which implies that their distinct actin organization may influence how their spheroids grow and develop. Vacuole-like structures, consistent with those seen in histology, are clearly visible at the later time point. In the T24 spheroids, actin fibers are evident on day 3 but become less prominent on day 14, although the cytoskeleton remains organized. The nuclei in both both T24 and HT1376 spheroids appear slightly smaller on day 14, potentially reflecting maturation or compaction processes.

Together, these results provide some insight into the nature of the discrepancies between the AFM and HFS measurements. AFM appears most sensitive to increased superficial features. Cell density and cellular elongation in the outer shell contribute to the shift towards solid-like behavior, but are not necessarily tied to a stiffening (see HCV29 *vs.* T24 spheroids). Compaction occurs predominantly in the outer region, accompanied by notable collagen deposition beneath the surface. This may explain why stiffness increases over time without major changes in damping behavior or transition frequency, as the ECM is beyond the volume probed by the AFM tip. HFS, given its pipette diameter of about 50 μm, averages the response of a local cell cluster (see Fig. 1-b) that reaches beyond the edge of the spheroid and into its deeper sections. This measurement therefore integrates contributions from multiple cell layers. However, the presence of collagen below the surface does not translate into stiffening at the microscale, likely due to its insufficient crosslinking or ineffective load-bearing role during suction-based HFS. These differences in probing depth help explain why structural heterogeneity observed in histology, such as variations in cell aspect ratio between outer and inner regions, does not translate directly into consistent mechanical trends across AFM and HFS measurements. Given that epithelial cells are highly dependent on cadherin-mediated adhesions, which may be weaker than integrin-based adhesions, the subsurface matrix may act as a mechanical weak point during bulk deformation.

In contrast, HT1376 spheroids exhibit minimal outer compaction and no collagen deposition, but still show increased stiffness in AFM measurements. This occurs despite the lack of significant cytoskeletal alignment, as nuclear aspect ratios remain largely unchanged. The stiffening could be attributed to cell-intrinsic changes associated with proliferation history, a

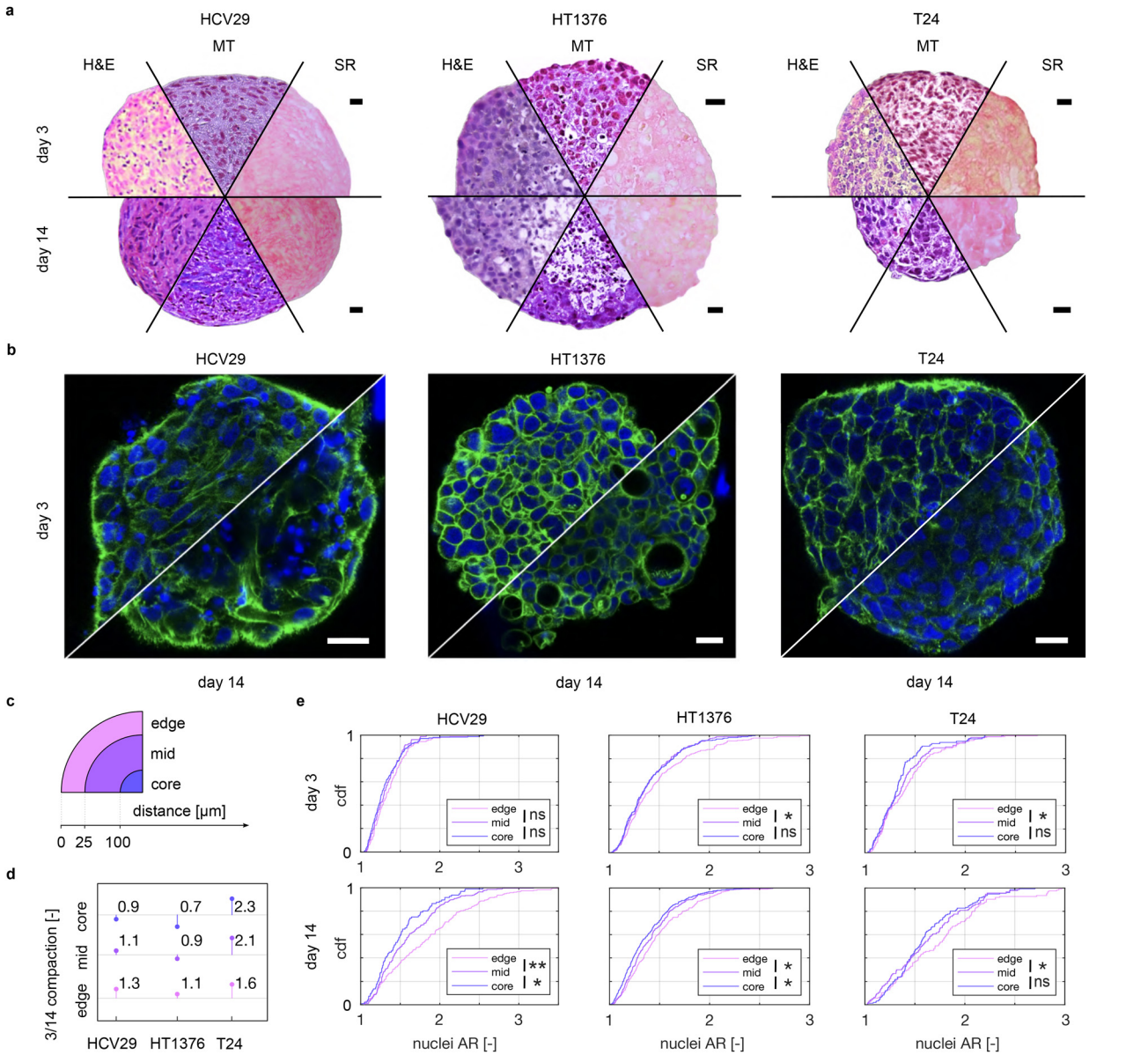

Fig. 5 Structural evolution of the three spheroid types over time. (a) Histological staining of the spheroids: hematoxylin & eosin (H&E), Masson trichrome (MT), and Sirius Red (SR). Spheroid cross-sections at two time culture points are shown. (b) Confocal images showing the organization of actin cytoskeleton inside spheroids. Green: F-actin, stained with phalloidin conjugated with Alexa Fluor 488, blue: nuclei, stained with Hoechst 33342. (c) Schematic subdivision of the spheroids in three regions: edge, mid, and core, as a function of the distance from the surface. (d) Compaction over time, per layer and by line, measured as the ratio between the number of nuclei per μm^2 at 14 over 3 days. (e) Empirical cumulative distribution functions (cdf) showing the aspect ratio distribution of the nuclei, categorized in three characteristic zones inside the spheroids. Significance based on Mann–Whitney U test, with $*p < 0.05$, $**p < 0.0005$. All scale bars are 20 μm. The extended versions of the histological staining and confocal images are illustrated in Fig. S7–S9.

phenomenon reported in other epithelial models.[62,63] However, on the microscale, this effect is barely noticeable, with a minimal change c_α and mainly an increase in viscosity. This is likely driven by structural degradation and vacuolization, which create mechanically weak regions and reduce the effective stiffness measured by suction. The vacuoles and emerging necrotic zones may promote fluidization at higher frequencies, as dead or loosely organized cells contribute little to the overall mechanical resistance. In effect, the measured HFS response is averaging a cortical layer and a necrotic area that does not provide load bearing capacity.

In T24 spheroids, superficial collagen is present on day 3 but disappears on day 14, while cell density and elongation in the outer region increase markedly. These two events may have an opposing effect in terms of superficial stiffness, which is why AFM showed no stiffening, but rather a reduced dependence of E' on frequency. The mechanical behavior becomes more solid-like, with a rise in the transition frequency and a decrease in the frequency-dependent viscous losses. This suggests that the maturing cytoskeletal architecture, possibly supported by better-aligned cortical actin and increased cadherin-based adhesions, contributes to greater resistance to deformation, even if the absolute

Table 2 Summary of the structural evolution of the three spheroid models under study, and their emergent rheological behavior. In italic, standout rheological traits evident in AFM data (nanoscale, cortical effects), and in bold standout rheological traits evident in HFS data (microscale, cellular cluster effects)

Cell line	Cadherin type	Changes in time (3–14 days)	Rheological maturation traits
HCV29	N-cadherin	– Compaction, cell elongation – Actin condensation – Sub-surface collagen deposition	– *Superficial stiffening* – **Overall tissue softening** – **Low frequency solidification**
HT1376	E-cadherin	– Minimal cell elongation – Significant growth – Necrotic core, vacuolization	– *Superficial stiffening* – **High frequency fluidization**
T24	N-cadherin	– Strong compaction, cell elongation – Loss of cortical actin – Minimal collagen loss	– *Shift to solid-like behavior* – **Low frequency fluidization**

modulus values remain unchanged. The enhanced elongation of the outer-layer cells could improve surface-to-volume ratios and allow for more adhesion contacts, thus stiffening the construct in a frequency-dependent manner. At the cluster level, the most evident effect is that of a reduced viscosity, reflecting the malignancy of the line. The springpot term c_α, associated with a more elastic response, increases marginally. This is in line with the explanation provided above, as a very small amount of superficial collagen is likely not detectable by HFS.

Across all lines, a key insight is that micro- and nanoscale mechanical properties do not always correlate directly with compaction or collagen content. Compaction and elongation in the outer shell do not necessarily yield higher stiffness at the nanoscale but instead correlate better with a transition toward solid-like behavior. We summarize the structural evolution and characteristic rheological traits in Table 2. Furthermore, microscale measurements appear relatively insensitive to compaction in absolute terms, as highlighted by the T24 spheroids. However, mechanical signatures on both scales are sensitive to reorganization between cells, even if the underlying mechanism remains partially elusive. Ultimately, these observations underscore the complex, multi-factorial nature of mechanical evolution in spheroids and highlight the limitations of simplified isotropic models in fully capturing their dynamics.

4 Conclusions

In this work, we investigate the rheological signature of three cancer spheroid lines, HCV29, HT1376, and T24. We studied their response as a function of scale (cell and cluster) and time over the course of two weeks. Although brightfield microscopy can suggest general morphological changes, such as compaction, it is insufficient to capture critical features, such as necrosis, extracellular matrix (ECM) deposition, or spatial heterogeneity. Similarly, observations from histological and immunofluorescence staining cannot be directly translated into mechanical behavior, underscoring the need for quantitative biomechanical profiling.

Our results show that nano- and microscale mechanical measurements offer complementary insights. Atomic force microscopy (AFM) highlights surface-level changes such as local compaction and cytoskeletal remodeling with the highest level of sensitivity. Hydraulic force spectroscopy (HFS) captures the integrated mechanical response of deeper spheroid regions, but can also measure cytoskeletal alterations. While alternative approaches such as AFM with large probes, parallel plate compression,[64] or bioindenters[65] could in principle be used to access bulk-like properties, these methods are limited by commercial availability, constraints on probe geometry, contact mechanics assumptions, and boundary conditions. In contrast, HFS enables characterization of the global mechanical response by decoupling tested volume and applied load, while avoiding uncertainties related to contact area and probe-sample interactions. In the present study this is particularly intuitive when looking at asymmetries in the internal structure of HCV29 or HT1376 (Fig. S8 and S9): the simultaneous probe-sample and sample substrate contact could lead to significant errors in the data interpretation.[66] Importantly, the apparent discrepancies between the AFM and HFS findings reflect true mechanical heterogeneity—both radially and temporally—arising from differential cell–cell contacts, ECM accumulation, and necrotic remodeling. These spatially resolved differences are particularly evident in epithelial-like lines (*e.g.*, HCV29), where collagen deposition and actin remodeling are confined to the outer layers, and in HT1376 spheroids, where necrotic cores reduce central stiffness. The discrepancy in the creep and DMA results in terms of viscous losses warrants future studies that focus on active remodeling during mechanical testing.

Placed in the context of previous rheological studies on spheroids, our results highlight how interpretation of stiffness trends is not easily generalizable, as competing mechanisms at the subcellular, cellular, and tissue level can result in a wide array of different behaviors. Similarly to observations from tissue-scale studies using complementary methods, including spheroid fusion and collective migration analyses, our data support the coexistence of cytoskeletal power-law relaxation at the cellular level and interface-dominated fluidisation at longer timescales. The quantitative agreement of the high-frequency transition range with previous AFM reports, together with the consistent viscosity ranking observed across spheroid fusion and HFS, further supports the physical relevance of the multiscale interpretation proposed here and the ability of rheological marker to provide some consistent interpretations. Our series model captures key trends with excellent fit quality which serves as phenomenological foundation, with Palade *et al.*'s (2024)[67] multiphase framework a natural future extension using our ECM/cadherin/single-cell data for 3D predictions.

The approach we present in this study can help explain overall tissue behavior. Integrating nanoscale and microscale rheology with structural imaging provides a robust framework to dissect the evolving mechanics of tumor spheroids. Our data also highlight the need for space-resolved mechanical characterization in 3D models. The current HFS architecture enables such measurement, and will be the focus of our future work. The ability to extract depth-resolved viscoelastic parameters in a label-free manner could be particularly useful for evaluating compounds targeting adhesion molecules (*e.g.* natalizumab,[68] vedolizumab[69]) or aimed at disrupting tissue architecture, as well as evaluating the penetration and effect of drugs affecting cytoskeletal properties.[70]

Author contributions

K. G.: conceptualization, methodology, investigation, formal analysis, visualization, writing – original draft. M. B.: conceptualization, methodology, investigation, hardware, software, formal analysis, visualization, writing – original draft. G. P. F.: investigation, formal analysis, writing – review and editing. J. P.: investigation, formal analysis, writing – review and editing. B. I. A.: writing – reviewing and editing. M. L.: funding acquisition, writing – reviewing and editing.

Conflicts of interest

M. B. is employed at Optics11 Life B.V. Optics11 Life B.V. holds for a patent on the HFS apparatus, where M. B. is listed as inventor.

Data availability

All data supporting the findings of this study are included in the manuscript and the supplementary information (SI). Supplementary information is available. See DOI: https://doi.org/10.1039/d6sm00020g.

Additional raw data files are available from the corresponding author upon reasonable request.

Acknowledgements

This work was financially supported by the H2020 European Research and Innovation Programme under the Marie Skłodowska-Curie grant agreement ''Phys2BioMed'' contract no. 812772.

Notes and references

1 K. H. Vining and D. J. Mooney, *Nat. Rev. Mol. Cell Biol.*, 2017, **18**, 728–742.
2 O. Chaudhuri, J. Cooper-White, P. A. Janmey, D. J. Mooney and V. B. Shenoy, *Nature*, 2020, **584**, 535–546.
3 M. Eroles and F. Rico, *J. Mol. Recognit.*, 2023, **36**(8), e3022.
4 D. Soteriou, M. Kubánková, C. Schweitzer, R. López-Posadas, R. Pradhan, O.-M. Thoma, A.-H. Györfi, A.-E. Matei, M. Waldner, J. H. W. Distler, S. Scheuermann, J. Langejürgen, M. Eckstein, R. Schneider-Stock, R. Atreya, M. F. Neurath, A. Hartmann and J. Guck, *Nat. Biomed. Eng.*, 2023, **7**, 1392–1403.
5 R. A. Burian, T. Appenzeller, P. Oertle, C. Raez, R. Y. Lim, S. Forte, S. Dellas, E. Obermann and M. Plodinec, *J. Clin. Oncol.*, 2017, **35**, 11618.
6 R. Burian, A. Jizawi, G. Zihlmann, T. Appenzeller, P. Oertle, C. Raez, R. Y. Lim, S. Forte, S. Dellas, S. Muenst, T. Vlajnic, E. Obermann, M. Ricci, K. Grimm, F. Niedermann, M. Loparic and M. Plodinec, *Cancer Res.*, 2019, **79**, 3140.
7 J. R. Ramos, J. Pabijan, R. Garcia and M. Lekka, *Beilstein J. Nanotechnol.*, 2014, **5**, 447–453.
8 E. Canetta, A. Riches, E. Borger, S. Herrington, K. Dholakia and A. K. Adya, *Acta Biomater.*, 2014, **10**, 2043–2055.
9 M. Lekka, J. Pabijan and B. Orzechowska, *Biochim. Biophys. Acta, Gen. Subj.*, 2019, **1863**, 1244–1254.
10 K. Gnanachandran, S. Kedracka-Krok, J. Pabijan and M. Lekka, *J. Biomech.*, 2022, **144**, 111346.
11 C. Jensen and Y. Teng, *Front. Mol. Biosci.*, 2020, **7**, 33.
12 O. Habanjar, M. Diab-Assaf, F. Caldefie-Chezet and L. Delort, *Int. J. Mol. Sci.*, 2021, **22**, 12200.
13 S.-Y. Lee, I.-S. Koo, H. J. Hwang and D. W. Lee, *SLAS Discovery*, 2023, **28**(4), 119–137.
14 B. Darvishi, M. R. Eisavand, K. Majidzadeh-A and L. Farahmand, *Br. J. Cancer*, 2022, **126**, 1253–1263.
15 R. J. Murphy, A. P. Browning, G. Gunasingh, N. K. Haass and M. J. Simpson, *Commun. Biol.*, 2022, **5**, 91.
16 E. Fröhlich, *Curr. Pharm. Des.*, 2020, **26**, 2137–2148.
17 E. C. Costa, A. F. Moreira, D. de Melo-Diogo, V. M. Gaspar, M. P. Carvalho and I. J. Correia, *Biotechnol. Adv.*, 2016, **34**, 1427–1441.
18 L. Guillaume, L. Rigal, J. Fehrenbach, C. Severac, B. Ducommun and V. Lobjois, *Sci. Rep.*, 2019, **9**, 6597.
19 R. C. Boot, G. H. Koenderink and P. E. Boukany, *Adv. Phys.:X*, 2021, **6**, 1978316.
20 Y. M. Efremov, I. M. Zurina, V. S. Presniakova, N. V. Kosheleva, D. V. Butnaru, A. A. Svistunov, Y. A. Rochev and P. S. Timashev, *Biophys. Rev.*, 2021, **13**, 541–561.
21 L. Andolfi, S. L. Greco, D. Tierno, R. Chignola, M. Martinelli, E. Giolo, S. Luppi, I. Delfino, M. Zanetti, A. Battistella, G. Baldini, G. Ricci and M. Lazzarino, *Acta Biomater.*, 2019, **94**, 505–513.
22 M. Berardi, K. Gnanachandran, J. Jiang, K. Bielawski, C. W. Visser, M. Lekka and B. I. Akca, *Soft Matter*, 2023, **19**, 615–624.
23 C. O'Toole, V. Stejskal, P. Perlmann and M. Karlsson, *J. Exp. Med.*, 1974, **139**, 457–466.
24 J. Bubeník, M. Barešová, V. Viklický, J. Jakoubková, H. Sainerová and J. Donner, *Int. J. Cancer*, 1973, **11**, 765–773.
25 S. Rasheed, M. B. Gardner, R. W. Rongey, W. A. Nelson-Rees and P. Arnstein, *J. Natl. Cancer Inst.*, 1977, **58**, 881–890.
26 X. Shi, *et al.*, *Mol. Cancer*, 2022, **21**, 37.
27 M. Berardi, K. Bielawski, N. Rijnveld, G. Gruca, H. Aardema, L. van Tol, G. Wuite and B. I. Akca, *Commun. Biol.*, 2021, **4**, 610.
28 A. Bonfanti, J. L. Kaplan, G. Charras and A. Kabla, *Soft Matter*, 2020, **16**, 6002–6020.

29 P. Bühlmann, *Stat. Sci.*, 2002, **17**, 52–72.
30 R. C. Boot, A. Roscani, L. van Buren, S. Maity, G. H. Koenderink and P. E. Boukany, *Lab Chip*, 2023, **23**(7), 1768–1778.
31 J. Kaplan, A. Bonfanti and A. Kabla, *J. Open Source Software*, 2019, **4**, 1700.
32 U. Schmidt, M. Weigert, C. Broaddus and G. Myers, *Cell Detection with Star-Convex Polygons*, 2018, pp. 265–273.
33 R. Zhao, K. L. Sider and C. A. Simmons, *Acta Biomater.*, 2011, **7**, 1220–1227.
34 A. Rigato, A. Miyagi, S. Scheuring and F. Rico, *Nat. Phys.*, 2017, **13**, 771–775.
35 J. S. de Sousa, R. S. Freire, F. D. Sousa, M. Radmacher, A. F. B. Silva, M. V. Ramos, A. C. O. Monteiro-Moreira, F. P. Mesquita, M. E. A. Moraes, R. C. Montenegro and C. L. N. Oliveira, *Sci. Rep.*, 2020, **10**, 4749.
36 D. Tsvirkun, J. Revilloud, A. Giannetti and C. Verdier, *J. Biomech.*, 2022, **141**, 111229.
37 P. Pravincumar, D. L. Bader and M. M. Knight, *PLoS One*, 2012, **7**, e43938.
38 K. Guevorkian, D. Gonzalez-Rodriguez, C. Carlier, S. Dufour and F. Brochard-Wyart, *Proc. Natl. Acad. Sci. U. S. A.*, 2011, **108**, 13387–13392.
39 K. Guevorkian and J. L. Maître, *Methods Cell Biol.*, 2017, **139**, 187–201.
40 M. Pandey, B. Zhu, K. Roach, Y. J. Suh, J. E. Segall, C.-Y. Hui and M. Wu, *Soft Matter*, 2026, **22**, 1618–1629.
41 P. H. Wu, D. R. B. Aroush, A. Asnacios, W. C. Chen, M. E. Dokukin, B. L. Doss, P. Durand-Smet, A. Ekpenyong, J. Guck, N. V. Guz, P. A. Janmey, J. S. Lee, N. M. Moore, A. Ott, Y. C. Poh, R. Ros, M. Sander, I. Sokolov, J. R. Staunton, N. Wang, G. Whyte and D. Wirtz, *Nat. Methods*, 2018, **15**, 491–498.
42 J. Rother, H. Nöding, I. Mey and A. Janshoff, *Open Biol.*, 2014, **4**, 140046.
43 J. Alcaraz, L. Buscemi, M. Grabulosa, X. Trepat, B. Fabry, R. Farré and D. Navajas, *Biophys. J.*, 2003, **84**, 2071–2079.
44 F. Liu, B. Gao, L. Lei, S. Liu, H. Li and M. Guo, *Nat. Phys.*, 2025, **21**, 1311–1318.
45 Y. Lai and Y. Hu, *Soft Matter*, 2017, **13**, 852–861.
46 J. Cacheux, J. Ordonez-Miranda, A. Bancaud, L. Jalabert, D. Alcaide, M. Nomura and Y. T. Matsunaga, *Sci. Adv.*, 2023, **9**, adf9775.
47 M. E. Pallarès, I. Pi-Jaumà, I. C. Fortunato, V. Grazu, M. Gómez-González, P. Roca-Cusachs, J. M. de la Fuente, R. Alert, R. Sunyer, J. Casademunt and X. Trepat, *Nat. Phys.*, 2023, **19**(2), 279–289.
48 M. Yu, A. Mahtabfar, P. Beelen, Y. Demiryurek, D. I. Shreiber, J. D. Zahn, R. A. Foty, L. Liu and H. Lin, *Biophys. J.*, 2018, **114**, 2703–2716.
49 T. Fuhs, F. Wetzel, A. W. Fritsch, X. Li, R. Stange, S. Pawlizak, T. R. Kießling, E. Morawetz, S. Grosser, F. Sauer, J. Lippoldt, F. Renner, S. Friebe, M. Zink, K. Bendrat, J. Braun, M. H. Oktay, J. Condeelis, S. Briest, B. Wolf, L.-C. Horn, M. Höckel, B. Aktas, M. C. Marchetti, M. L. Manning, A. Niendorf, D. Bi and J. A. Käß, *Nat. Phys.*, 2022, **18**, 1508–1516.
50 G. Dechristé, J. Fehrenbach, E. Griseti, V. Lobjois and C. Poignard, *J. Theor. Biol.*, 2018, **454**, 102–109.
51 N. V. Kosheleva, Y. M. Efremov, B. S. Shavkuta, I. M. Zurina, D. Zhang, Y. Zhang, N. V. Minaev, A. A. Gorkun, S. Wei, A. A. Shpichka, I. N. Saburina and P. S. Timashev, *Sci. Rep.*, 2020, **10**, 22133.
52 D. Oriola, M. Marin-Riera, K. Anlaş, N. Gritti, M. Sanaki-Matsumiya, G. Aalderink, M. Ebisuya, J. Sharpe and V. Trivedi, *Soft Matter*, 2022, **18**, 3771–3780.
53 R. C. Boot, A. van der Net, C. Gogou, P. Mehta, D. H. Meijer, G. H. Koenderink and P. E. Boukany, *Sci. Rep.*, 2024, **14**, 1–14.
54 S. Ongenae, H. Svitina, T. E. Belpaire, J. Vangheel, T. Martens, P. V. Berghe, I. Papantoniou and B. Smeets, *Nat. Commun.*, 2025, **16**, 10467.
55 M. von Dassow, J. A. Strother and L. A. Davidson, *PLoS One*, 2010, **5**, e15359.
56 A. Chatterjee, P. Kondaiah and N. Gundiah, *Biomech. Model. Mechanobiol.*, 2022, **21**, 553–567.
57 X. Li, Q. Ni, X. He, J. Kong, S. M. Lim, G. A. Papoian, J. P. Trzeciakowski, A. Trache and Y. Jiang, *PLoS Comput. Biol.*, 2020, **16**, e1007693.
58 F. Pérez-Verdugo and S. Banerjee, *PRX Life*, 2023, **1**, 023006.
59 I. Smyrek, B. Mathew, S. C. Fischer, S. M. Lissek, S. Becker and E. H. K. Stelzer, *Biol. Open*, 2018, **8**, bio037051.
60 T. Zisis, D. B. Brückner, T. Brandstätter, W. X. Siow, J. d'Alessandro, A. M. Vollmar, C. P. Broedersz and S. Zahler, *Biophys. J.*, 2022, **121**, 44–60.
61 M. Lekka, D. Gil, W. Dabroś, J. Jaczewska, A. J. Kulik, J. Lekki, Z. Stachura, J. Stachura and P. Laidler, *J. Mol. Recognit.*, 2011, **24**, 833–842.
62 M. Zambito, F. Viti, A. G. Bosio, I. Ceccherini, T. Florio and M. Vassalli, *Nanomaterials*, 2023, **13**, 1190.
63 I. Dulińska-Molak, M. Pasikowska, K. Pogoda, M. Lewandowska, I. Eris and M. Lekka, *Int. J. Pept. Res. Ther.*, 2014, **20**, 77–85.
64 P. Marmottant, A. Mgharbel, J. Käfer, B. Audren, J.-P. Rieu, J.-C. Vial, B. van der Sanden, A. F. M. Marée, F. Graner and H. Delanoë-Ayari, *Proc. Natl. Acad. Sci. U. S. A.*, 2009, **106**, 17271–17275.
65 N. Antonovaite, M. Berardi, K. Bielawski and N. Rijnveld, in *3.2 Fiber-Optics-Based Nanoindenters*, ed. M. Lekka, D. Navajas, M. Radmacher and A. Podestà, De Gruyter, Berlin, Boston, 2023, pp. 129–146.
66 M. Glaubitz, N. Medvedev, D. Pussak, L. Hartmann, S. Schmidt, C. A. Helm and M. Delcea, *Soft Matter*, 2014, **10**, 6732–6741.
67 C. Verdier and L. I. Palade, *EPL*, 2024, **145**, 17001.
68 L. Steinman, *Nat. Rev. Drug Discovery*, 2005, **4**, 510–518.
69 L. Besendorf, T. M. Müller, C.-I. Geppert, I. Schneider, L. Mühl, I. Atreya, F. Vitali, R. Atreya, M. F. Neurath and S. Zundler, *Ther. Adv. Gastroenterol.*, 2022, **15**, 17562848221098899.
70 A. Kubiak, M. Chighizola, C. Schulte, N. Bryniarska, J. Wesolowska, M. Pudelek, M. Lasota, D. Ryszawy, A. Basta-Kaim, P. Laidler, A. Podestà and M. Lekka, *Nanoscale*, 2021, **13**, 6212–6226.